NANO MICRO small

Supporting Information

for *Small,* DOI: 10.1002/smll.202201674

Gecko Adhesion on Flat and Rough Surfaces: Simulations with a Multi-Scale Molecular Model

Tobias Materzok, Danna De Boer, Stanislav Gorb, and Florian Müller-Plathe*

SUPPORTING INFORMATION

Gecko Adhesion on Flat and Rough Surfaces: Simulations with a Multi-scale Molecular Model

Tobias Materzok Danna De Boer Stanislav Gorb* Florian Müller-Plathe**

Tobias Materzok, Danna De Boer, Prof. Dr. Florian Müller-Plathe
Email Addresses: t.materzok@theo.chemie.tu-darmstadt.de, f.mueller-plathe@theo.chemie.tu-darmstadt.de
Eduard-Zintl-Institut für Anorganische und Physikalische Chemie and Profile Area Thermofluids and Interfaces
Technische Universität Darmstadt
Alarich-Weiss-Str. 8
D-64287 Darmstadt
Germany
Prof. Dr. Stanislav Gorb
Email Address: sgorb@zoologie.uni-kiel.de
Zoological Institute Functional Morphology and Biomechanics
Kiel University
Am Botanischen Garten 1-9
D-24118 Kiel
Germany

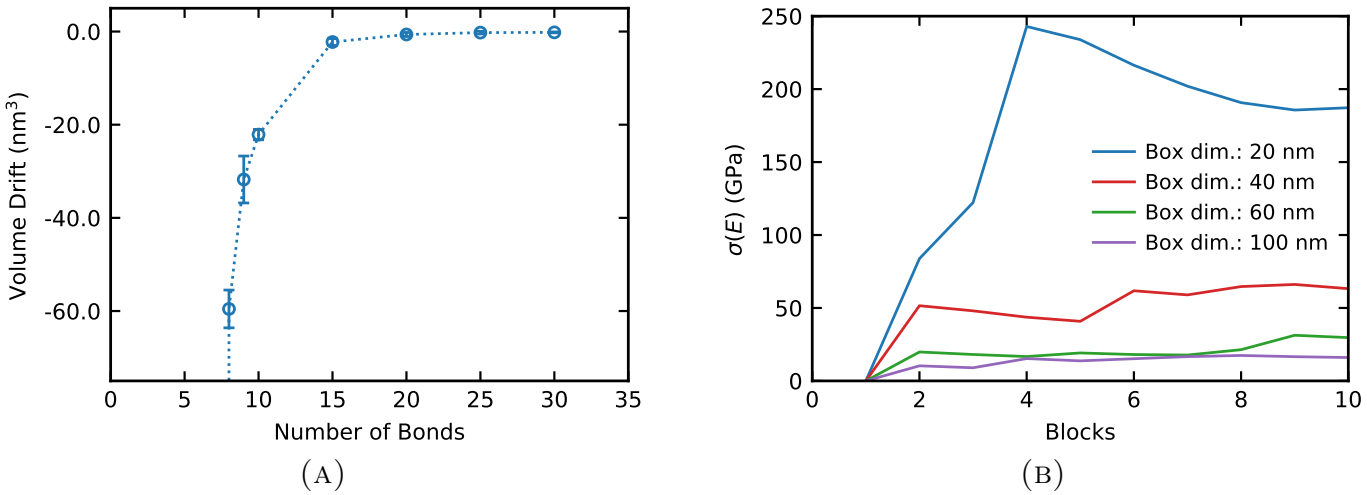

Figure S1: (A) Volume drift (or change) of keratin bulk material in the NPT ensemble (1 bar, 300 K) over 200 ns simulation time against the bond number with an initial system size of $60 \cdot 60 \cdot 60$ nm. The average is computed from 10 independent samples and the standard deviation of the mean is used as the error. (B) Convergence of the standard deviation of the Young's modulus $\sigma(E)$ against the number of independent simulations used for averaging and, in different colors, the system sizes that were tested. 30 bond neighbors are used for these simulations. A system size of $60 \cdot 60 \cdot 60$ nm with 30 bonds neighbors is sufficiently large.

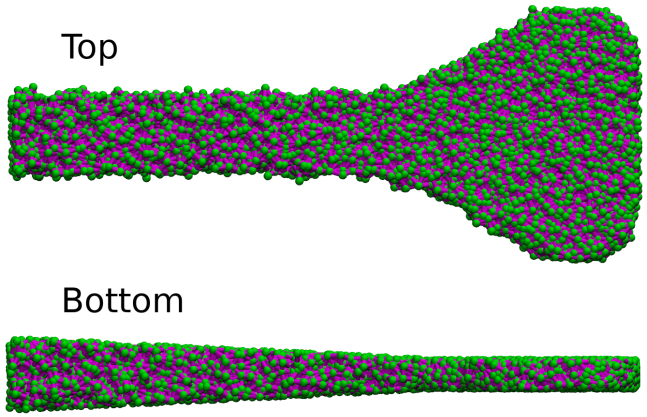

Figure S2: (Top) The top-viewing perspective of the spatula. Spatula beads are shown in green and a visual representation of the bond network is shown in purple. (Bottom) The shape of the spatula from its side is inspired by the finite element model of Sauer et al.[1] and the finite element calculations of Xu et al.[2]

Vertex	x (nm)	y (nm)	Vertex	x (nm)	y (nm)
1	0.000	82.780	62	0.000	92.780
2	0.000	60.900	61	0.000	114.660
3	22.680	61.330	60	22.680	114.230
4	44.160	61.080	59	44.160	114.480
5	66.780	61.310	58	66.780	114.250
6	89.140	61.550	57	89.140	114.010
7	113.090	61.540	56	113.090	114.020
8	138.600	62.230	55	138.600	113.330
9	163.710	62.470	54	163.710	113.090
10	188.760	62.100	53	188.760	113.460
11	213.790	62.450	52	213.790	113.110
12	237.290	62.260	51	237.290	113.300
13	256.460	59.770	50	256.460	115.790
14	273.290	55.720	49	273.290	119.840
15	287.650	50.800	48	287.650	124.760
16	302.490	45.000	47	302.490	130.560
17	317.480	37.370	46	317.480	138.190
18	332.730	26.260	45	332.730	149.300
19	347.200	17.070	44	347.200	158.490
20	362.240	8.890	43	362.240	166.670
21	376.230	2.460	42	376.230	173.100
22	390.260	0.360	41	390.260	175.200
23	402.970	0.000	40	402.970	175.560
24	415.000	2.270	39	415.000	173.290
25	423.820	6.910	38	423.820	168.650
26	430.010	13.090	37	430.010	162.470
27	434.190	20.690	36	434.190	154.870
28	437.410	30.860	35	437.410	144.700
29	438.180	44.000	34	438.180	131.560
30	438.960	61.000	33	438.960	114.560
31	439.730	81.800	32	439.730	93.760

Table S1: All 62 vertices of our mesoscale spatula model.

Name	Extent (relative to l_x of spatula)	Color in Figure 1
Spatula pad	70% to 100%	blue
Shaft haft	0% to 5%	grey
Spatula tip	95% to 100%	red
Spatula joint	60% to 65%	purple
x_s	65%	-

Table S2: Names, colors and the position of different areas of the mesoscale spatula model. The extent is relative to the spatula length in the x direction l_x.

1 Surface model details

The surface is generated much like the bulk keratin model, it has the same random arrangement of beads and the same bead density. We use the same minimum distance between beads and the same target density to fill the simulation box up to a maximum height z_m with beads. The minimum height of the surface is always 13 nm. In the case of rough surfaces, we insert beads underneath a three-dimensional landscape defined by $z_m = 13\ \text{nm} + \lambda \sin(x \cdot \pi n_p / l_x^s + \pi X_x) \cdot \sin(y \cdot \pi n_p / l_y^s + \pi X_y)$ with the peak height $\lambda = 8$ nm, the number of peaks in x and y direction n_p, and the length of the surface in x and y: l_x^s and l_y^s. We apply a random phase shift using a uniformly distributed random number $X \sim U([0, 2])$ in the x and y directions to simulate random placements of the spatula on top of a surface.

2 Details about the parameterization of the anisotropic bonded interactions of the mesoscale keratin force field

Before parameterizing the bond coefficients k and k_b, the ideal bulk keratin system size is determined by applying strain of 0, 1, and 2% in the (virtual) fibril direction for ten independently created bulk keratin systems of different sizes. For each system, Young's modulus is calculated. This is done by increasing box lengths, as shown in Figure S1 (B). By ideal bulk system size, we mean here that computation is expeditious and that the average and standard deviation of Young's modulus E are converged. No finite-size effects affect our force field parameterization, and statistics are distinct enough to distinguish between fitting or unfitting parameters. For each system size, Young's modulus along the (virtual) fibril direction E is calculated for all ten systems, and the smallest system size at which the standard deviation of Young's modulus is converged is chosen. As seen in Figure S1 (B), a system size of $(60)^3$ nm is sufficiently large and is used from here on out for all simulations of Young's modulus and Poisson's ratio.

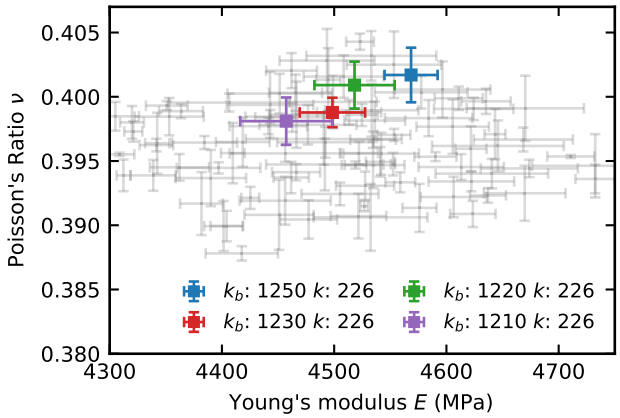

Figure S3: Resulting Poisson's ratios ν and Young's moduli E of the bulk keratin material system of the combination of k and k_b values (listed in Table S3). The standard deviation using three samples for averaging (grey) and 10 samples (colored) are used as the error. The bond coefficients labeled in the legend are in units of kJ mol^{-1} nm^{-2}. Grey data points are listed in Table S3. The average is computed from 10 independent samples and the standard deviation of the mean is used as the error.

k (kJ mol^{-1} nm^{-2})	k_b (kJ mol^{-1} nm^{-2})	E (MPa)	$\sigma(E)$ (MPa)	ν	$\sigma(\nu)$
220	1150	4229.89	11.34	0.399	0.001
220	1250	4523.01	12.37	0.404	0.001
230	1150	4308.66	13.32	0.396	0.000
230	1250	4596.50	42.65	0.401	0.002
235	1150	4312.27	6.13	0.394	0.001
235	1250	4584.15	38.98	0.398	0.001
240	1150	4338.86	20.17	0.394	0.001
240	1250	4645.88	58.69	0.396	0.002
245	1150	4401.44	17.26	0.390	0.002
245	1250	4643.31	9.31	0.397	0.002
255	1150	4404.21	14.41	0.390	0.001
255	1250	4673.84	43.26	0.394	0.001
260	1150	4417.73	32.20	0.388	0.001
260	1250	4732.51	17.59	0.394	0.001
223	1250	4553.27	42.13	0.402	0.003
223	1230	4508.45	35.65	0.402	0.002
223	1220	4451.48	46.55	0.400	0.002
223	1210	4442.88	38.58	0.399	0.003
229	1250	4577.57	41.32	0.400	0.001
229	1230	4499.05	38.81	0.400	0.002
229	1220	4513.33	28.54	0.399	0.001
229	1210	4476.64	43.26	0.398	0.002

Table S3: A small selection of results of the bulk keratin material parametrization of the anisotropic bond coefficients k and k_b. The Young's modulus E is calculated between 0% and 2% strain in the direction of the (virtual) fibrils, and the Poisson's ratio ν is the average between 1% and 2% strain orthogonal to the fibril direction. The values are averages over 3 independently generated systems.

3 Details about the parameterization of the nonbonded interactions of the mesoscale keratin force field

We compare different system sizes to ensure that finite-size effects are negligible. Figure S4 shows that p converges slowly with increasing system size. For the smallest system of $30 \cdot 30$ nm (blue), each bead is bonded to $N_{\text{bonds}}/N = 8.6\%$ of all beads, leading to finite-size effects. For a system of size $90 \cdot 90$ nm, the ratio of bonds to the number of beads is only 0.9%. We continue with this size since it is a good compromise of the value of p with computational efficiency.

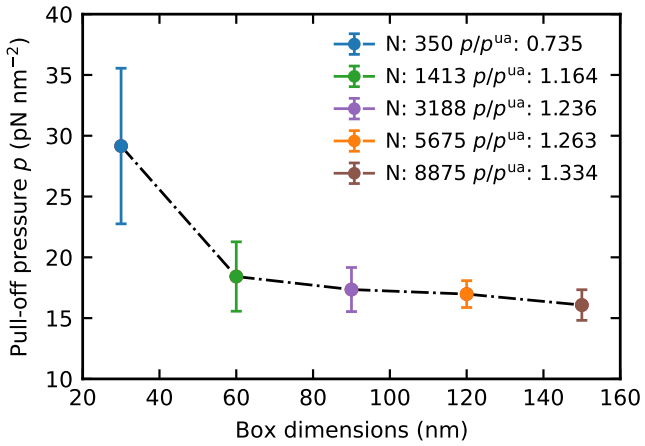

Figure S4: Pull-off pressure of different sized bulk keratin systems ranging from 30 nm box length (total number of beads $N = 350$) to 150 nm ($N = 8875$). With an increasing number of beads, the average and the standard deviation of the pull-off pressure converges. The ratio of the bulk keratin pull-off pressure to the all-atom pull-off pressure p/p^{ua} is shown in the legend. The force field parameters used for this validation are $k = 226$ kJ mol^{-1} nm^{-2}, $k_b = 1220$ kJ mol^{-1} nm^{-2}, $\sigma = 2.8$ nm, and $\epsilon = 1000$ kJ mol^{-1}. The average is computed from 10 independent samples and the standard deviation of the mean is used as the error.

4 United-atom gecko keratin model

The united-atom (UA) gecko keratin model uses the GROMOS 54A7 force field for all atoms present in the system, keratin protein and surface[3, 4, 5, 6].

In earlier coarse-grained work[7] we discovered that only the intrinsically disordered protein regions (IDRs) of the gecko keratin directly contact the surface and not the beta-folded region of the keratin protein that polymerizes into nanofibrils. Thus only the IDRs of the gecko keratin protein are responsible for the adhesive energetic interaction between spatula and surface. Therefore we amorphized a gecko beta-keratin protein (Ge-cprp-9), where only the intrinsically disordered parts of the protein are considered.

The exact equilibration protocol, including energy minimization, amorphization at 2000 K with subsequent cool down, and multi-step equilibrations in the NPT ensemble with and without soft-core potentials, would go beyond the scope of this SI.

Additionally, gecko keratin contains a large fraction of disulfide bonds.[8, 7] We cross-link one-third of the cysteines ($\approx 7.5\%$ of the amino acids in the protein). Therefore, achieving the same cross-link density as in a previous coarse-grained work.[8]

The united-atom keratin simulations of the previous work were carried out using the GROMACS 2018 software package[9]. The production runs to calculate Young's modulus were performed in three-dimensional periodic boundary conditions (PBC). The timestep was 2 fs, and a velocity rescale[10] thermostat kept the temperature at 300 K. A semi-isotropic Berendsen[11] barostat with a compressibility of $4.5 \cdot 10^{-5}$ bar^{-1} in x and y, and a compressibility of 0 bar^{-1} in z, kept the pressure of the system at 1 bar. Production runs were repeated five times for five independently generated systems ($n = 25$). Young's modulus was computed with a linear fit to the first 1% strain. Poisson's ratio was computed as the average over strain 1% to 5%.

5 Simulation details

All simulations are carried out using the GROMACS 2018 and 2021 software packages[9]. The van der Waals interaction cutoff is 12 nm, and van der Waals interactions are modeled using the 12-6 Lennard-Jones potential. We use the potential-shift-Verlet scheme[12] as a cutoff modifier for a physically[13] smooth transition at the cutoff. We simulate state points in NVT and NPT with a temperature of 300 K and a pressure of 1 bar, respectively. Different thermostats and barostats are used at different stages; see the following subsections. The timestep is 20 fs.

5.1 Mechanical property calculations with the mesoscale keratin material

Young's modulus and Poisson's ratio are calculated for the three-dimensionally periodic mesoscale keratin material by scaling the initial system configuration in (virtual) fibril direction to give strains of 0 to 2%.

A semi-isotropic Berendsen barostat[11] with a compressibility of 0 bar^{-1} in the fibril direction keeps the pressure at 1 bar using a coupling time of $\tau_p = 100$ ps and allows the perpendicular dimensions to adjust. A velocity rescale thermostat[10] is used with a coupling time of $\tau_T = 2$ ps. The systems are simulated for 200 ns. Pressure, density, and bond energies converge during the first nanosecond of the simulation. The last 180 ns are assumed to be in equilibrium and are used for the analysis of mechanical properties.

5.2 Mesoscale keratin material detachment simulations

To perform mesoscale keratin material detachment simulations, the material with the optimized parameters (Section 3) is placed on top of a surface of height 13 nm with a minimum distance between surface and bulk of $\sigma = 4.0$ nm. The fibril direction is parallel to the surface. The PBC in directions parallel to the surface makes the mesoscale keratin material and surface semi-infinite, i.e., two infinite plates in adhesive contact. The surface beads are fixed in place. The center of mass (COM) of the beads of the top half of the bulk keratin is connected by a harmonic bond to a virtual particle, which can be moved at will and which mimics the action of a cantilever.

The pulling simulations of the mesoscale keratin material periodic parallel to the surface are performed in three consecutive steps. First, the keratin material is preloaded (i.e., pressed against the surface) with a constant pressure of 0.2553 kJ mol^{-1} nm^{-3} (corresponding to a constant force of 2068 kJ mol^{-1} nm^{-1} in the $90 \cdot 90$ nm system) acting on the top half of the material for 100 ns (red particles in Figure 5). Next, the system is allowed to relax for 100 ns with no external force applied. Finally, the keratin material is pulled away from the surface in the direction normal to the surface. To this end, the virtual cantilever is moved away from the surface with constant velocity $v = 0.001$ nm ps^{-1} (with the harmonic force constant $k_{\text{pull}} = 1000$ kJ mol^{-1} nm^{-2} or $k_{\text{pull}} = 1660$ pN nm^{-1}), with the virtual particle located initially at the COM of the top half of the keratin. The resulting loading rate, $\dot{F} = k_{\text{pull}} v = 1.66 \cdot 10^{12}$ pN s^{-1}, is equal to the loading rate of the united-atom reference simulations[14].

The preload and relax phases use a stochastic dynamics (SD) thermostat[15] with a coupling time of $\tau_T = 1$ ps to inhibit any possibility of the harmonic keratin network to periodically oscillate without being able to dissipate the energy. The final pulling simulation, when the virtual cantilever moves away from the surface to pull off the bulk keratin material, uses a velocity rescale thermostat[10] with $\tau_T = 1$ ps, because the friction of the SD thermostat would bias the measured pull-off force. All simulations take place in the NVT ensemble with a large vacuum volume above the keratin to allow the pull-off.

6 Spatula detachment simulations

Initially, the spatula is generated as described in Section 2.2. Then we push the spatula pad beads (Figure 1 blue and Table S3) for 100 ns with a constant pressure of 0.2553 kJ mol^{-1} nm^{-3} against the surface. The surface beads are fixed in space. The center of mass (COM) of the shaft haft, designated as the first five percent (in x dimension, with the shaft haft coming before the spatula pad) of the spatula length ($l_x \cdot 0{-}5\%$), as seen in Figure 1 (grey) and described in Table S3, is kept from rotating around the axis normal to the surface by a flat-bottom[16, 17] potential (as implemented in GROMACS[9]) with $k_{\text{flat-bottom}} = 2 \cdot 10^4$ kJ mol^{-1} nm^{-2}, the distance where the potential starts is $r_0 = 2$ nm. After this preload step, the system is allowed to relax with no applied forces for another 100 ns. A flat-bottom[16, 17] potential is, however, still used to restrict the spatula from rotating around the axis normal to the surface.

In the fourth step, the spatula is prepared to be bent upwards. Therefore, we move the shaft haft COM away from the surface for 300 ps with $k_{\text{pull}} = 1 \cdot 10^5$ kJ mol^{-1} nm^{-2} and a velocity of 0.1 nm ps^{-1}. Simultaneously, the shaft haft is kept from rotating as described above. This step is done to correct a GROMACS specific error that arises when the spatula initially bends opposite of the set bending direction (due to thermal fluctuations).

As done by Sauer et al.[1], the main pulling mechanism is broken into two parts: bending the shaft so that it has an inclination of some degree to the surface (step 5), and then pulling the spatula vertically off that surface (step 6). The bending is carried out by applying an umbrella potential ($V(\theta) = k/2\,(\theta - \theta_0)^2$ with $k = 5 \cdot 10^9$ kJ mol^{-1} rad^{-2}) on the COM of the spatula shaft haft using an "angle-axis" geometry. This is GROMACS terminology for an angle-dependent harmonic potential between two vectors. Here, one vector is defined between two COMs, and the second vector is defined by an axis. The angle-axis is defined between the shaft haft COM and the spatula tip COM (Table S3) and the vector parallel to the surface $\{-1, 0, 0\}$. We rotate with 0.001 deg ps^{-1} upwards (Note that the angle-force constant is in units of radians, while the unit for the rate of bending is expressed in degree, as used in GROMACS). This pulling results in a force normal (upwards) to the shaft bending the spatula along the way.

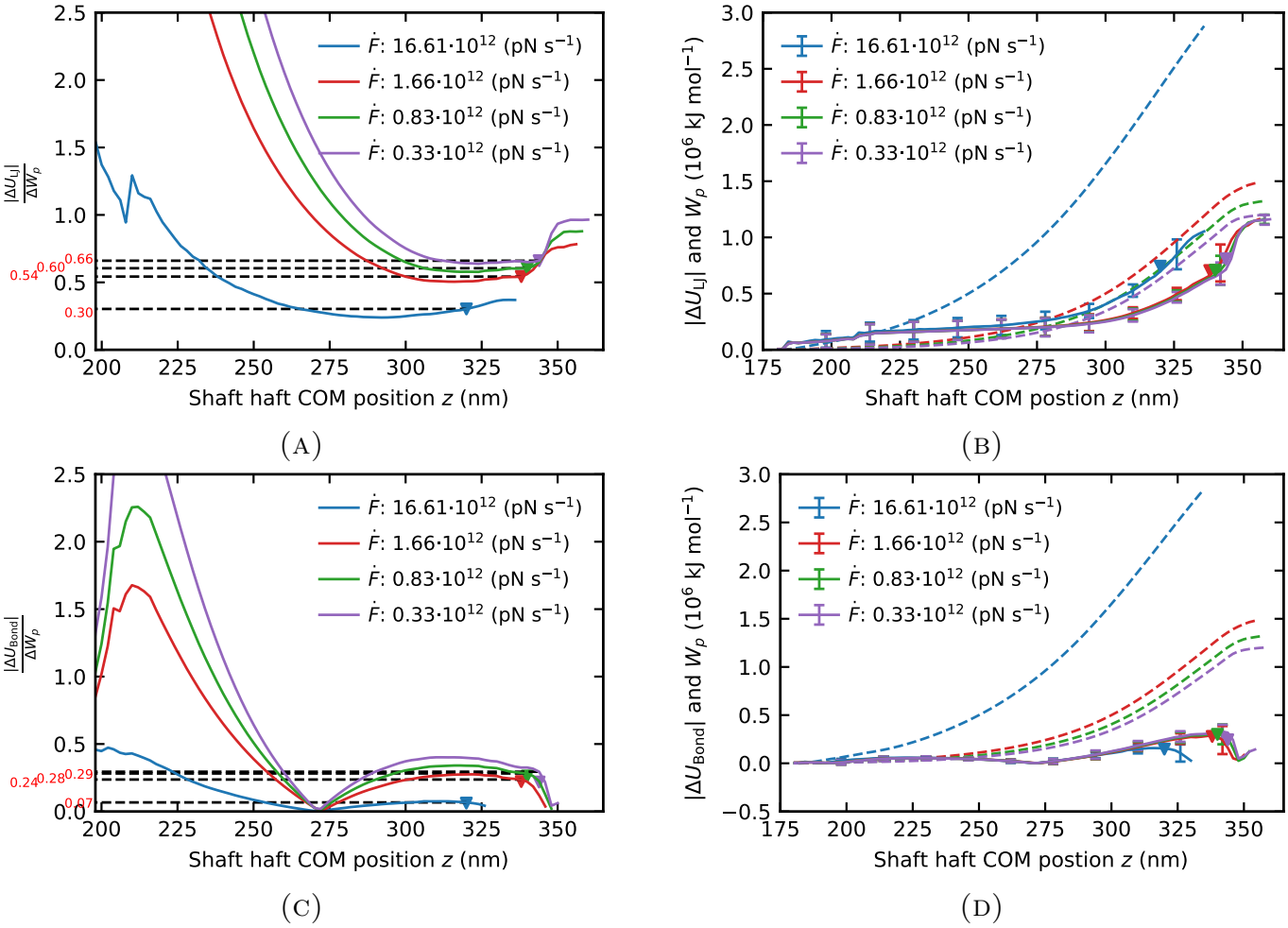

Figure S5: (A) Ratio of adhesive energy overcome during detachment to work of pull-off for different loading rates. The position of the shaft haft when the force is at its maximum (pull-off) is marked with a triangle. Red values at the beginning of black dashed lines note the ratio at the position of pull-off. (B,D) Energies (solid lines) and work (dashed lines) shown side-by-side for the varying loading rates. (C) Ratio of bending energy to work of pull-off. Data shown is the average computed from 10 independent samples.

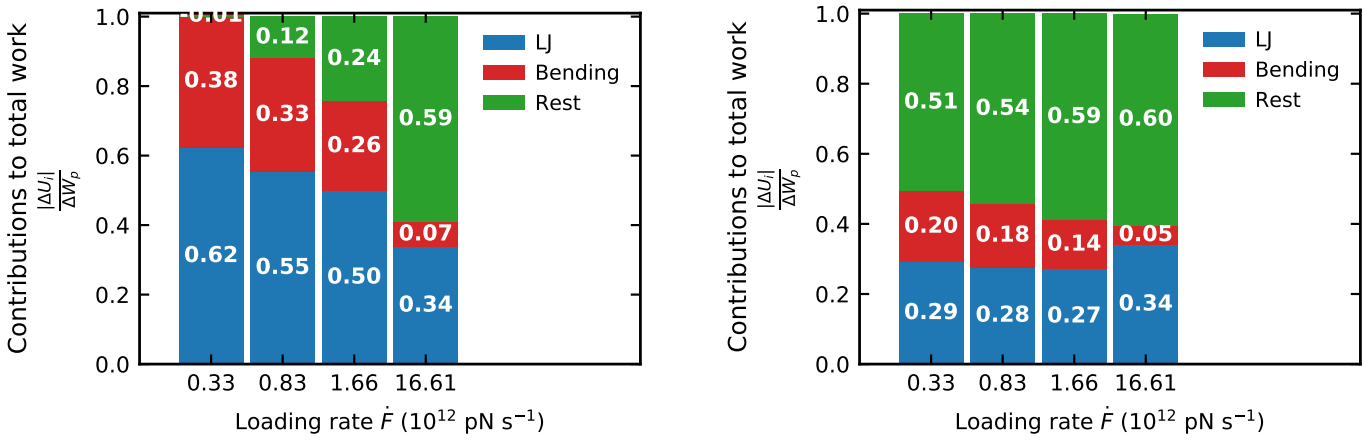

(A) (B)

Figure S6: The ratio of overcome adhesive energy (blue) at the position of the maximum force is compared to contributions overcome from bending (red) and dissipated rest (green) energies to work of pull-off for different loading rates. The ratios are annotated in the stacked bars. The spatula equilibrium inclination is $\theta_S = 60°$ (A) and (B) $\theta_S = 75°$. The average is computed from 10 independent samples.

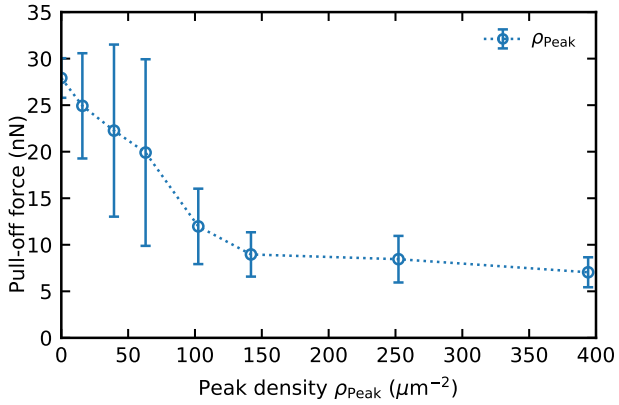

Figure S7: The pull-off force is shown against the peak (or valley) density. The data points are the average computed from 10 independent samples and the standard deviation of the mean is used as the error.

References

[1] R. A. Sauer, M. Holl, *Comput. Methods Biomech. Biomed. Eng.* **2013**, *16*, 6 577.

[2] Q. Xu, Y. Wan, T. S. Hu, T. X. Liu, D. Tao, P. H. Niewiarowski, Y. Tian, Y. Liu, L. Dai, Y. Yang, Z. Xia, *Nat. Commun.* **2015**, *6*, 1 8949.

[3] L. D. Schuler, X. Daura, W. F. v. Gunsteren, *J. Comput. Chem.* **2001**, *22*, 11 1205.

[4] C. Oostenbrink, A. Villa, A. E. Mark, W. F. V. Gunsteren, *J. Comput. Chem.* **2004**, *25*, 13 1656.

[5] N. Schmid, A. P. Eichenberger, A. Choutko, S. Riniker, M. Winger, A. E. Mark, W. F. van Gunsteren, *Eur. Biophys. J.* **2011**, *40*, 7 843.

[6] W. Huang, Z. Lin, W. F. van Gunsteren, *J. Chem. Theory Comput.* **2011**, *7*, 5 1237.

[7] T. Materzok, S. Gorb, F. Müller-Plathe, *Soft Matter* **2022**, *18*, 6 1247.

[8] K. S. Endoh, T. Kawakatsu, F. Müller-Plathe, *J. Phys. Chem. B* **2018**, *122*, 8 2203.

[9] B. Hess, C. Kutzner, D. van der Spoel, E. Lindahl, *J. Chem. Theory Comput.* **2008**, *4*, 3 435.

[10] G. Bussi, D. Donadio, M. Parrinello, *J. Chem. Phys.* **2007**, *126*, 1 014101.

[11] H. J. C. Berendsen, J. P. M. Postma, W. F. van Gunsteren, A. DiNola, J. R. Haak, *J. Chem. Phys.* **1984**, *81*, 8 3684.

[12] S. Páll, B. Hess, *Comput. Phys. Commun.* **2013**, *184*, 12 2641.

[13] D. van der Spoel, P. J. van Maaren, *J. Chem. Theory Comput.* **2006**, *2*, 1 1.

[14] T. Materzok, A. Canestraight, S. N. Gorb, F. Müller-Plathe, *Nat. Commun.* **2022**, under review.

[15] N. Goga, A. J. Rzepiela, A. H. de Vries, S. J. Marrink, H. J. C. Berendsen, *J. Chem. Theory Comput.* **2012**, *8*, 10 3637.

[16] G. M. Clore, M. Nilges, D. K. Sukumaran, A. T. Brünger, M. Karplus, A. M. Gronenborn, *EMBO Rep.* **1986**, *5*, 10 2729.

[17] H. Ryu, T.-R. Kim, S. Ahn, S. Ji, J. Lee, *PLOS ONE* **2014**, *9*, 10 e108888.

Table of Contents

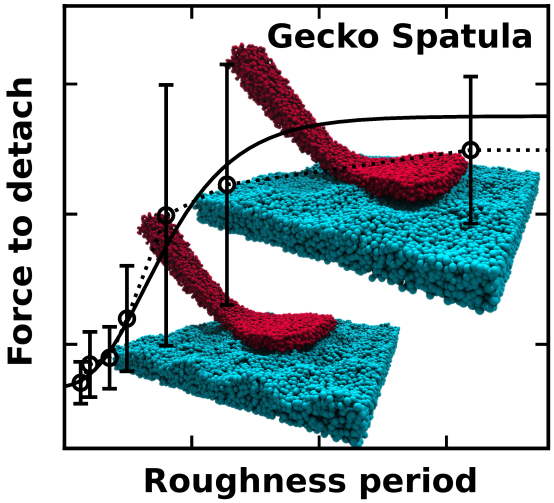

A multiscale modeling approach derives a particle-based mesoscale gecko spatula model that is able to link atomistic and mesoscale simulations and yield pull-off forces similar to experimental work. A root-mean-square roughness causality is disproven and a roughness wavelength-dependent sigmoidal trend is revealed, instead. We confirm an experimental hypothesis.